

Ultrashort Echo Time Magnetic Resonance Fingerprinting (UTE-MRF) for Simultaneous Quantification of Long and Ultrashort T₂ Tissues

Qing Li¹, Xiaozhi Cao¹, Huihui Ye^{1,2}, Congyu Liao¹, Hongjian He¹, and Jianhui Zhong^{1,3}

¹ Center for Brain Imaging Science and Technology, Key Laboratory for Biomedical Engineering of Ministry of Education, College of Biomedical Engineering and Instrumental Science, Zhejiang University, Hangzhou, Zhejiang, China

² State Key Laboratory of Modern Optical Instrumentation, College of Optical Science and Engineering, Zhejiang University, Hangzhou, Zhejiang, China

³ Department of Imaging Sciences, University of Rochester, Rochester, USA

Corresponding author: Jianhui Zhong (email: jzhong3@gmail.com)

Submit to *Magnetic Resonance in Medicine* as a *Full Paper*

Word count: 4924

Key words: ultrashort echo time, magnetic resonance fingerprinting, sinusoidal TE variation, amplitude demodulation, and pseudo-CT image

Abstract

Purpose: To demonstrate an ultrashort echo time magnetic resonance fingerprinting (UTE-MRF) method that can simultaneously quantify tissue relaxometries for muscle and bone in musculoskeletal systems and tissue components in brain and therefore can synthesize pseudo-CT images.

Methods: A FISP-MRF sequence with half pulse excitation and half spoke radial acquisition was designed to sample fast T_2 decay signals. Sinusoidal echo time (TE) pattern was applied to enhance MRF sensitivity for tissues with short and ultrashort T_2 values. The performance of UTE-MRF was evaluated via simulations, phantoms, and in vivo experiments.

Results: A minimal TE of 0.05 ms was achieved in UTE-MRF. Simulations indicated that extension of TE sampling increased T_2 quantification accuracy in cortical bone and tendon, and had little impact on long T_2 muscle quantifications. For a rubber phantom, an average T_1/T_2 of 162/1.07 ms from UTE-MRF were compared well with gold standard T_2 of 190 ms from IR-UTE and T_2^* of 1.03 ms from UTE sequence. For a long T_2 agarose phantom, the linear regression slope between UTE-MRF and gold standard was 1.07 ($R_2=0.991$) for T_1 and 1.04 ($R_2=0.994$) for T_2 . In vivo experiments showed the detection of cortical bone and Achilles tendon, where the averaged T_2 was respectively 1.0 ms and 15 ms. Scalp images were in good agreement with CT.

Conclusion: UTE-MRF with sinusoidal TE variations shows its capability to produce pseudo-CT images and simultaneously output T_1 , T_2 , proton density, and B_0 maps for tissues with long T_2 and short/ultrashort T_2 in the brain and musculoskeletal system.

Introduction

Magnetic resonance imaging (MRI) provides exquisite contrast in soft tissues. However, bone, tendon, meniscus, and myelin sheath that have short or ultrashort T_2 values (in the order of 1-10ms) are barely detectable in conventional MRI (1–3). Ultrashort echo time (UTE) and zero echo time (ZTE) imaging techniques have been used to detect these constituents (4–6). Due to their long scan time, single-point (7,8) and multi-point (9) imaging techniques are rarely used for in vivo studies. To increase k-space coverage efficiency, center-out readout trajectories like radial and spiral were employed (10–13), associated with half-pulse slice selective excitation for 2D imaging and non-selective hard pulse excitation for 3D imaging.

Quantitative UTE (qUTE) imaging have shown extensive applications in diagnosing cartilage degeneration (14), meniscus tear (15), age-related cortical bone deterioration and osteoporosis (16). Cortical bone water concentration, a new metric for the quality of human cortical bone, requires both T_1 and T_2^* relaxometries. However, separate acquisitions of T_1 and T_2^* maps typically take more than an hour (1). To reduce scan time, Abbasi-Rad et al. quantified T_1 using dual TR method and employed an experiential T_2^* value (16). However, the individual differences in T_2^* values between healthy volunteers and patients were lost.

UTE and ZTE techniques are not only applied in MRI system to diagnose musculoskeletal diseases, but also in positron emission tomography (PET)/MRI system to produce pseudo-CT (pCT) images for PET attenuation correction (AC). Bone contrast is enhanced by suppressing background long T_2 signals using e.g., long T_2 saturation pulse (17,18), short T_2 selective double inversion recovery preparation (19), or image subtraction at two echo times (20). Wiesinger et al. obtained pCT images by segmenting proton density (PD) map using ZTE (4). Since soft tissue, bone, and air possess different relaxometries and PDs, simultaneous characterization of multiple tissue properties would be beneficial for highlighting bone structures.

Magnetic resonance fingerprinting (MRF) (21) that simultaneously quantifies multiple tissue properties could benefit the characterization of bone. Different tissue properties like T_1 , T_2 , T_2^* , and PD are incorporated into the signal evolutions induced by changing flip angle (FA), repetition time (TR), and echo time (TE). In addition, MRF has shown reasonable quantification results and potential clinical applications in human brain and abdomen compared to gold standards (22,23). However, challenges remain in using MRF to quantify tissues containing ultrashort T_2 components. First, since the original MRF method has a minimum echo time of several milliseconds, ultrashort T_2 / T_2^* tissues are barely detected. Second, low proton density in ultrashort T_2 tissue causes high noise level in MRF signal evolutions which degrades accuracy for MRF dictionary matching. Third, to avoid T_2^* blurring, an acquisition window of $0.81T_2$ was recommended for 2D imaging (24), which constrained the acquisition window length of cortical bone to sub-millisecond. Fourth, the undersampling artifact from a MRF frame reconstructed using a radial spoke is more severe than using conventional spiral acquisition (25).

In this work, an ultrashort echo time MR fingerprinting (UTE-MRF) method was proposed to address the problems listed upon. The proposed method was based on a fast imaging with steady-state precession (FISP) sequence, which has been demonstrated in previous MRF studies (26). In the proposed UTE-MRF sequence, sinc excitation pulses of all TRs were replaced by self-refocused half pulses (27,28). Together with the half-spoke radial readout, the minimum echo time was reduced to 0.05 ms. The variation of FAs and TEs from TR to TR was introduced to generate fingerprint-like signal evolutions for long, short, and ultrashort T_2 tissues. Multiple repetitions (reps) of UTE-MRF acquisitions were performed to increase SNR for ultrashort T_2 tissues. Simulations, phantom studies, and in vivo studies were performed to test the proposed UTE-MRF method on aspect of tissue quantifications and pCT image synthesis.

Methods

Pulse sequence design

As a proof of concept, we demonstrated a 2D UTE-MRF method shown in Fig. 1 based on FISP-MRF sequence (26). To reduce the echo time, half pulse sinc excitation was implemented together with the positive/negative polarized slice selection gradient. A bipolar slice selection was used to reduce impact of eddy current (29). A MRF unit contained series of 480 image acquisitions with variable FAs, TEs, and golden angle rotated radial trajectory. FA pattern consisted of four half-period sin waves, whose peak FAs were 32° , 22° , 60° , and 10° and the minimum FA was 5° . TR was fixed at 6 ms to shorten scan time. Slice selection gradient polarization was changed between odd and even MRF units to achieve complete slice selection (12,27). A waiting time of 3 s was applied after MRF unit 1 to recover spin to their initial state before MRF unit 2. Since short and ultrashort T_2 tissues had low proton density, 5 reps was used to limit the scan time within in a minute (56 s) for phantom, ankle, and brain imaging. And additional repetition was performed to increase SNR for bone quantification, leading to a scan time of 68 s for leg imaging. Among repetitions, radial trajectories at the same UTE-MRF frame were uniformly distributed over a unit circle.

Direct B_0 map estimation from the phase of MRF frames

Echo time variations were applied in previous MRF studies to either increase T_2^* sensitivity (30) or to separate water and fat signals (31). In this study, we employed TE variations to increase MRF sensitivity for short and ultrashort T_2 tissues. Fig. 2 shows signal evolutions of six tissue constituents (under the same T_1 of 180 ms but increased T_2 values of 0.5, 1, 2, 5, and 10 ms) simulated with extended phase graph (EPG) (32,33) and FA pattern in Fig. 1b. Intuitively, normalized signal evolutions under constant TEs

(first two columns in Fig. 2) are difficult to be differentiated, even when TE is minimized to 0.05 ms. Sinusoidal TE sampling (from 0.05 to 2 ms) increases signal evolution differences. However, variable TE causes a spatial and temporal dependent phase based on field offset and TE. To prevent those phase disturbances, Benedikt et al. only used the magnitude of both measured data and dictionary entries (30). Instead of losing the phase information, off-resonance induced phase error was corrected by either employing a pre-scanned B_0 map (34), or incorporating the B_0 effects into MRF dictionary via modelling the field inhomogeneity (31). However, these methods added extra computation in MRF dictionary generation and matching processes.

To avoid increasing dictionary computation and matching burden, we demonstrated a dictionary free B_0 estimation method based on sinusoidal TE pattern. This idea is inspired by the amplitude modulation and demodulation which has been widely employed in communication system (35). Phase accumulated in MRF image series are modulated by field offset B_{off} and sinusoidal TE carrier wave $(\alpha \sin(\omega\tau) + \beta)$,

$$Phase = 2\pi i \cdot B_{off} \cdot (\alpha \sin(\omega\tau) + \beta) + n, \quad [1]$$

where B_{off} is the frequency offset (unit: rad) caused by field inhomogeneity and chemical shift; α , β , and ω are TE sampling parameters, $\alpha = (TE_{max} - TE_{min})/2$, $\beta = (TE_{max} + TE_{min})/2$, ω is the frequency of sinusoidal waveform; τ is the time vector $[1, 2, \dots, F]^T$ (unit: TR); and n represents the noise term. To estimate B_{off} , accumulated phase in [1] is demodulated via multiplying the carrier wave $\sin(\omega\tau)$,

$$dPhase = (2\pi i \cdot B_{off} \cdot (\alpha \sin(\omega\tau) + \beta) + n) \cdot \sin(\omega\tau). \quad [2]$$

$dPhase$ is then derived as

$$dPhase = 2\pi i \cdot B_{off} \cdot \alpha \cdot \left(\frac{1+\cos(2\omega\tau)}{2}\right) + (2\pi i \cdot B_{off} \cdot \beta + n) \cdot \sin(\omega\tau). \quad [3]$$

The noise term n in [3] comprises physiological, thermal, and other MRI system related noise. However, since phase maps are reconstructed from single k-space interleave at each TR, noise n consists mostly of data undersampling aliasing. Cao et al. employed a temporal sliding window method to increase scan efficiency based on

the slow phase variations in FISP-MRF (36). Similarly, to reduce k-space undersampling induced phase noise, a sliding window matrix S is applied and multiplied from both sides of [3],

$$S \cdot dPhase = 2\pi i \cdot S \cdot B_{off} \cdot \alpha \cdot \left(\frac{1 - \cos(2\omega\tau)}{2} \right) + S \cdot (2\pi i \cdot B_{off} \cdot \beta + n) \cdot \sin(\omega\tau) \quad [4]$$

where S is a $F \times F$ array, containing values of either 0 or 1. Each row at S behaves as a window. Only when the element is within the window, its value is 1, otherwise 0. From the first row to the last row in S , the window moves from left to right. For a sliding window matrix with window size of 4, we have S in the form of

$$S = \begin{pmatrix} 1 & 1 & 1 & 1 & 0 & \cdots & 0 & 0 \\ 0 & 1 & 1 & 1 & 1 & \cdots & 0 & 0 \\ 0 & 0 & 1 & 1 & 1 & \cdots & 0 & 0 \\ & & & \vdots & & & & \\ 0 & 0 & 0 & 0 & 0 & \cdots & 1 & 1 \end{pmatrix}_{F \times F} \quad [5]$$

Due to the nature of the smoothed phase maps (shown in supplementary vedio), noise n shows little impact and is ignored after sliding window. Time integral among constant TE periods mT ($T = 2\pi/\omega$ and m is the number of periods) is employed as a lowpass filter, such that constant phase accumulations carried by $\cos(2\omega\tau)$ and $\sin(\omega\tau)$ are self-cancelled. Herein field offset B_{off} is derived,

$$B_{off} = \frac{2}{2\pi i \cdot \alpha \cdot mT} \cdot \sum_0^{mT} (S \cdot dPhase) \quad [6]$$

Image reconstruction

MRF dictionaries were generated under variable FAs in Fig.1b and sinusoidal TEs (TE_{min} = 0.05 ms and TE_{max} = [0.05:0.05:1.0] ms using EPG. Since our previous work demonstrated that TE variation period had little impact on ultrashort T₂ tissue quantification (37), TE variation period was set to 120 in the unit of MRF image frames. Dictionary T₁ values varied from 10 to 3000 ms, including [10:10:400, 400:20:2000, 2000:40:3000] ms. And T₂ values varied from 0.1 to 300 ms, including [0.1:0.1:5, 5:5:150, 150:10:300] ms. Dictionary entries were normalized. Similar to previous MRF studies, a resting time of 3 s was appended after MRF repetitions to

allow recovery of longitudinal magnetizations (38–40). Meanwhile, a two-step dictionary generation method was performed to achieve more accurate matching (39,40).

Parametric maps of T_1 , T_2 , PD, and B_0 were generated by four steps. First, multi-channel images were transformed from k-space into image space using inverse NUFFT (41) and combined using adaptive coil combination (42). Images from positive and negative excitations were directly complex summed. Second, B_0 map was estimated from MRF phase maps based on [6], where sliding window length of 20 was employed to balance the reduction of undersampling aliasing and tissue specificity lost. Meanwhile, phase maps from No. 240 to 480 frames (i.e., 2 TE variation periods) were used to avoid the superposition of IR induced phase inversion. Third, to remove phase accumulations induced by field inhomogeneity, complex MRF images from step 2 (under sliding window size of 20) were multiplied by the conjugate phase maps depending B_0 and TE. Fourth, image frames were normalized and matched with dictionary entries (21). Since cortical bone has low spin density and ultrashort T_2 , it is sensitive to bone marrow signal from radial undersampling artifact. Herein, we first employed partial volume dictionary matching method (43) to estimate and remove bone marrow components and then apply MRF dictionary matching to obtain cortical bone T_2 .

Since adiabatic IR pulse was implemented, MRF possessed an intrinsic advantage in long T_2 suppression near soft tissue IR-null point. Even though ultrashort T_2 relaxation time of bone makes it decay fast in the transverse plane, it recovers fast and shows longitudinally hyperintensity due to its short T_1 . With the calculated T_1 and T_2 maps, transvers and longitudinal magnetization maps at any MRF frame could be generated via looking up to the dictionary. The pCT images were obtained by selecting a proper frame in the longitudinal magnetizations where ultrashort T_2 bone was highlighted.

Simulation study

To investigate the impact of TE sampling range to tissue quantification accuracy, numerical simulations were carried out on a digital phantom (size of 110 x 110) shown in Fig. 3. Tissue components including muscle, tendon, and total water of bone were modeled and numbered from 1 to 3. Cortical bone free water was included as the fourth component. Dark space in the phantom was for air. Most of the tissue properties (listed in Fig. 3b) were chosen following the literatures (19,44,45). Ideal MRF frames were generated from MRF transverse magnetizations using EPG under FAs and TEs (Fig. 1b), T_1 , T_2 , and PD (Fig.3b). Although TE variation increased MRF short T_2 specifications, it caused a TE dependent T_2' weighting from MRF frame to frame. Therefore, T_2' effect was modeled by multiplying an exponential T_2' to ideal MRF frames. T_2' values in Fig. 3b were calculated via $1/(1/T_2^* - 1/T_2)$, where T_2^* was 25 ms for muscle, 2.3 ms for tendon, 0.7 ms for bone total water, and 2.4 ms for bone free water.

SNR variations were also considered. Complex white Gaussian noise was added to represent different SNR levels listed in Fig. 3b. k-Space samples were obtained point-by-point through forward NUFFT of the noised MRF frames, golden angle rotated radial readout (duration = 0.79 ms, where ramp time = 0.15 ms and plateau time = 0.64 ms) and corresponding density compensation function (46). TE_{min} was fixed at 0.05 ms and TE_{max} increased from 0.05 to 1 ms in steps of 0.05 ms. Multi-parametric maps were reconstructed following the method in image reconstruction section. Root-mean-square-error (RMSE) of measured T_1 and T_2 maps were calculated compared to gold standard T_1 and T_2 values listed in Fig. 3b.

Phantom and in vivo experiments

To test the proposed UTE-MRF method, experiments were conducted on a whole body

3T scanner (Magnetom Prisma, Siemens Healthineers, Erlangen, Germany). A home-made phantom with 8 tubes (mimicing soft tissues) and 4 rubber plugs (mimicing ultrashort T_2 tissues) was imaged using a 20-ch head coil. Seven of those tubes were filled with $MnCl_2$ of different concentrations to represent tissue components of variable T_1 and T_2 values, and the eighth tube was filled with oil. In vivo experiments were carried out under the approval of local institutional review board. A 26 year-old male volunteer participated in calf and tendon imaging using a 15-ch knee coil. Brain imaging was performed on a 55 year-old female volunteer using 64-ch brain coil. As a comparison, CT images (slice thickness = 1.0 mm and in plane resolution = $1.0 \times 1.0 \text{ mm}^2$) were acquired on a Philips iCT scanner (Brilliance iCT, Philips Healthcare, The Netherlands) at First Affiliated Hospital of Zhejiang University.

To achieve ultrashort TE, a 0.7 ms half pulse was employed, which was generated by dividing a 1.2 ms sinc pulse with time-bandwidth of 6 into 2 sub-pulses. VERSE algorithm (47) was applied to cool down the peak RF amplitude and corresponding interrupted slice selection gradient. With ramp sampling, the readout window was 0.79 ms (0.64 ms for plateau and 0.15 ms for ramp) and the readout bandwidth was 1780 Hz/pixel. To increase data incoherence and reduce eddy current effect, radial spokes were rotated in a small golden angle (23.62°) (48). Slice thickness was 6 mm for phantom and 7 mm for in vivo. $TE_{min} = 0.05 \text{ ms}$, $TE_{max} = 0.6 \text{ ms}$, and TE variation period = 120. To obtain a high quality pCT image, TE was minimized to 0.05 ms unchanged for brain scan. TR (6 ms), TD (3s), and resting time (3s) were used consistently throughout all the experiments. FAs in Fig. 1a were halved in brain imaging for potential safety consideration. Multi-parametric maps were reconstructed to achieve a resolution of $1.0 \times 1.0 \text{ mm}^2$ (matrix size of 240×240) for phantom, leg, and tendon and $0.75 \times 0.75 \text{ mm}^2$ (matrix size of 256×256) for brain using MATLAB R2014a (The MathWorks, Inc., Natick, MA) on a Linux (Red Hat Enterprise) server (with Core i7 Intel Xeon 2.8 GHz CPUs and 64GB RAM).

Inversion recovery UTE (IR-UTE) sequence was used to acquire gold standard T_1 map with multiple inversion time (TI) of 50, 100, 200, 400, and 800 ms, TR = 3000 ms, TE = 0.05 ms, and number of spokes = 248. Gold standard T_2^* map was generated from a UTE sequence with multiple TEs of 0.05, 0.2, 0.5, 1, 2, and 4 ms, TR = 1500 ms, number of spokes = 248. All the images acquired with IR-UTE and UTE sequence were reconstructed following the first step of MRF image reconstructions. Gold standard T_2 map was measured with spin echo (SE) sequence with TEs = 25, 50, 75, 100, and 125 ms, TR = 3000 ms, matrix size = 192 x 192, resolution = 1 x 1 mm², and 6/8 partial Fourier acquisition. The total acquisition time was 124 min for T_1 , 74 min for T_2^* , and 36 min for T_2 . T_1 , T_2 , and T_2^* maps were reconstructed using a toolbox in public domain (<http://www-mrsrl.stanford.edu/~jbarral/t1map.html>) (49).

Results

Simulation Results

Fig. 4 shows the simulation results of musculoskeletal tissue mimic phantom under 3 and 6 MRF reps. The impact of TE sampling range is quantified in Fig. 4a, where TE_{min} is fixed to 0.05 ms and TE_{max} increased from 0.05 to 1 ms, in steps of 0.05 ms. Overall, T_1 and T_2 RMSEs are decreased by about 2 times with doubled repetitions of acquisition. Muscle T_1 and T_2 quantifications are robust against TE variations even under repetitions of 3. Tendon and bone total water show an increased T_2 quantification accuracy with the extended TE sampling. Meanwhile, larger TE variations could benefit T_2 quantifications under smaller reps, which indicates expanding TE sampling range could increase the MRF sensitivity of short T_2 tissues against low SNR and undersampling aliasing. T_1 RMSEs are slightly increased from 33 / 17 / 77 ms to 36 / 21 / 82 ms for tendon / total water / free water under 6 reps. Free water shows the largest quantification errors due to its lowest PD. T_1 and T_2 maps reconstructed at $TE_{max} = 0.6$ ms are compared with gold standard T_1 and T_2 in Fig. 4b. Strong streaking artifacts are observed with 3 reps, especially in T_2 difference map. When repetition is increased to 6, T_2 quantification errors are substantially reduced, but T_2 biases are observed in

tendon and free water.

Phantom and In Vivo Results

Fig. 5 shows the comparisons of phantom measurements including T_1 , T_2 , PD, and off-resonance between gold standard and UTE-MRF. To highlight short T_2 components, T_2 maps are displayed in the range of 0 to 5 ms in the third column. PD maps are normalized by the intensity of oil (the bottom tube at each image). Each column shares the same display range shown at the bottom. T_1 , long T_2 , and PD maps from UTE-MRF sequences show comparable results with gold standards. Oil T_2 (about 120 ms) observed in UTE-MRF is approached to the T_2 of fat in the literatures (43), while it is underestimated in the gold standard method. T_2 values of rubber phantom in UTE-MRF are close to gold standard T_2^* . Strong frequency offset about 400 Hz is noted in the oil tube due to 3.5 ppm chemical shift.

Fig. 6 shows the comparisons of the quantification results in the chosen ROIs between UTE-MRF and gold standards. Twelve rectangular ROIs (12 x 8 pixels) are chosen among the phantom tubes shown in Fig.6a. T_2 from UTE-MRF (Fig.6a, last column) are compared with gold standard T_2^* for ultrashort T_2 rubber phantom (red markers) and with gold standard T_2 for other long T_2 agarose tubes (green markers). Dash line represents the identity line ($y = x$). T_1 and T_2 values from UTE-MRF show a good agreement with gold standard T_1 ($y = 1.07x - 43.71$, $R^2 = 0.991$) and T_2 for long T_2 agarose phantoms ($y = 1.04x - 3.27$, $R^2 = 0.994$). Fig. 6b lists T_1 and T_2 values of UTE-MRF from the chosen ROIs.

Fig. 7 shows in vivo ankle and leg results from UTE-MRF. Each column from left to right represents anatomic images, T_1 , long T_2 , short T_2 , PD, and off-resonance maps. Two ROIs (5 x 5) in bone marrow and muscle are marked by the red box shown in anatomic image. The mean T_1 / T_2 for bone marrow and muscle are respectively 364 /

141 ms and 1038 / 27 ms. Short T_2 tissues including tibia (labeled by *a*), fibula (*b*), Achilles tendon (*c*), and peroneus longus tendon (*d*) are observed in the fourth column under different display ranges. The averaged T_2 in a 3 x 3 ROI in Fig. 7 is found to be 1.0 ms for cortical bone and 15 ms for Achilles tendon. High off-resonance artifact is detected in bone marrow and skin due to the chemical shift between fat and water.

Fig. 8 shows simulation results in the brain for the longitudinal magnetization time evolution using T_1 and T_2 relaxometries reconstructed from UTE-MRF. Since tissue relaxometries are quantified through dictionary matching, one could look up the dictionary and generate transverse / longitudinal magnetization changes at any MRF time point. Longitudinal magnetization maps from MRF frame No. 130 and No. 393 are displayed at the bottom, where ultrashort T_2 bone is highlighted.

Fig. 9 shows brain parametric maps generated from in vivo data, including T_1 , T_2 , and PD. Pseudo-CT images produced by UTE-MRF are directly compared with CT images. To suppress soft tissues including white matter, gray matter, and scalp, pCT images are generated via dividing the M_z map from MRF frame No. 130 by T_1 map. Bone structures, including hyper intensity areas and Zygomatic bone, in pCT images as pointed with red arrows, are in good agreement with CT images.

Discussion

In this work, a UTE-MRF method was proposed to simultaneously quantify long and short / ultrashort T_2 tissues and to synthesize pCT images. Sinusoidal TE variation was incorporated in acquisition and library matching. Variable TE induced phase changes were compensated using B_0 map demodulated from the phases of MRF frames. TE in UTE-MRF was minimized to 50 μ s. T_1 , T_2 , and PD maps were reconstructed through dictionary matching. Longitudinal magnetization map, which was obtained via looking up the dictionary based on the quantified relaxometries, was employed to produce pCT

images. Simulation, phantom measurements, and in vivo studies showed the capability of UTE-MRF for detecting and quantifying musculoskeletal system mimic phantoms, tendon, cortical bone, and muscle. In vivo brain scans also demonstrated that UTE-MRF was capable of brain quantifications and producing pCT images.

With sinusoidal TE variation, B_0 map is directly estimated from the phase of MRF frames through amplitude demodulation method without additional dictionary and matching burden. In the image domain, TE variation causes a synchronized sinusoidal phase change to MRF frames. This phase change mathematically equals to the product of TE and B_0 offset caused by chemical shift and field inhomogeneity. In such a way, field variations are modulated into the phase of MRF frames. Calculating the field changes directly using [6] suffers from strong undersampling aliasing, resulting in poor field estimation. Herein, a non-iterative sliding window method (36) was used to reduce undersampling artifacts. Cao et al. chose the number of fully sampled spiral interleaves as the window length. For imaging FOV = 140 x 140 mm² and resolution = 1.0 x 1.0 mm², a fully sampled radial would require 220 spokes. However, a window length of 220 would tremendously decrease the tissue specificities, because it is about twice of TE and FA variation period (120). To balance tissue specificities and undersampling aliasing, a window size of 20 was used in this study, where the maximum TE variation within the sliding window was $(TE_{max} - TE_{min})/2$. Since multiple repetitions were performed to increase SNR for bone, tendon, and rubber phantom, the actual image undersampling factor within the sliding window was 2.2.

There is a tradeoff between B_0 sensitivity and image SNR in choosing TE sampling ranges. More accurate field estimation would be achieved through strong phase changes via increased TE variation. However, there is more loss in image SNR as a penalty due to the local field inhomogeneity effect. Among the acquired 480 MRF image frames containing 4 periods of sinusoidal phase variation, only phase maps from the last 2 periods were used to avoid the impact of IR induced phase changes along MRF frames.

The 2 periods (1440 ms, 2 x 120 x TR) is adequate for the tissue with longest T_1 to pass through its IR null point, e.g., for T_1 of 2000 ms, its IR null point is 1386 ms ($\ln(2) \times T_1$).

To achieve ultrashort TE for detection ultrashort T_2 components, half pulse excitation (duration of 0.7 ms) and radial acquisition (window length of 0.79 ms) were employed. Although T_2^* decay during excitation has an impact on the excitation profile, Pauly has shown that there is a small loss in signal and slightly broadening in slice profile for tissue with T_2 of 0.25 ms and a half pulse with 1 ms in duration (27). Since T_2^* effect is weaker under a shorter pulse duration of 0.7 ms compared with Pauly's case, we ignored the impact of T_2^* decay during excitation. Excitation performance would be degraded by eddy currents and timing mismatch between gradient and RF. To minimize these effects, we adjusted the timing between slice selection gradient and RF pulse. RF pulse was adjusted to perform a -10 to 10 μs (in steps of 1 μs) time shift relative to gradient. The optimal shift time of -3 μs was chosen based on performance of the slice selection profile. To decrease the impact of eddy currents, a bipolar slice selection gradient was employed based on the fact that the long term eddy currents from ramp-up and ramp-down gradients are cancelled due to their opposite polarities (29). However, residual short-term eddy currents may still distort slice selection gradient. A better slice selection performance could be achieved via measuring the trajectory of slice selection gradient as suggested by Manhard et al. (12). To reduce the T_2^* blurry of bone ($T_2 \leq 1$ ms), readout window of 0.79 ms was employed under optimal window size of $0.81T_2$ suggested by Rahmer et al. (25). Off-resonance blurry from bone marrow and scalp was limited by using high readout bandwidth of 1780 Hz/pixel.

Simulation results in Fig. 4 indicate that UTE-MRF is capable of simultaneously quantifying long and short T_2 tissue components. T_1 and T_2 quantification errors in muscle remain steady with increased TE sampling ranges, which suggests TE variations have little impact on long T_2 tissue. Since doubling sequence repetitions reduces $T_1 /$

T_2 RMSEs by about two-fold (Fig. 4a), radial undersampling artifact is probably the primary source for the steady quantification errors. Because TE sampling ranges are close to the T_2^* values of cortical bone and tendon, TE change-induced T_2' effects are more significant in cortical bone and tendon than in muscle. Herein, almost an uniform bias between gold standard T_2 and measured T_2 is observed in bone and tendon (Fig. 4b). Therefore, UTE-MRF quantifies T_2 for long T_2 soft tissues as reported in FISP-MRF method and T_2^* for short and ultrashort T_2 tendon and cortical bone. Even though cortical bone free water has longer T_2 values than bone total water and tendon, its quantification accuracy are the poorest due to its low proton density. At low image SNR under 3 UTE-MRF reps, an increment of TE sampling range could enhance MRF specificities to ultrashort T_2 tissues and benefit ultrashort T_2 tissue quantifications. Suggested by the simulation performance of short T_2 tissues, the optimal TE_{max} of 0.6 ms was used for phantom and in vivo experiments and TE_{min} of 0.05 ms was unchanged throughout the experiments.

For phantom quantifications in Fig. 6, most of relaxometries in UTE-MRF are in good agreement with gold standards except for the T_2 of oil tube. This is likely because fat in- and out-of- phase effect was not taken into account, when different TEs in SE sequence were chosen for gold standard T_2 mapping. Results from in vivo experiments indicated that Achilles tendon and cortical bone can be quantified using UTE-MRF. The averaged T_2 of cortical bone and tendon from chosen ROI is respectively 1.0 ms and 15.0 ms. Bicomponent analyses have shown that cortical bone possesses two T_2^* components, i.e., bound water with shorter T_2^* of 0.36 ms and free water with longer T_2^* of 5.56 ms (50). Tendon also shows a similar bicomponent characteristics with shorter T_2^* of 0.88 ms and longer T_2^* of 25.58 ms (51). Since the minimum TE was 0.05 ms, UTE-MRF acquires both bound water and free water in cortical bone and tendon. Therefore, UTE-MRF quantifies the total water for cortical bone and tendon, which is also supported by the simulation results of musculoskeletal system-mimic phantom.

The proposed UTE-MRF method has been tested via simulations, phantom, and in vivo experiments. However, there are some limitations in the current 2D UTE-MRF approach. First, imaging imperfections like B_1 inhomogeneity and non-ideal slice profile are not totally encompassed, which limit the quantification performance. To correct the B_1 inhomogeneity, B_1 maps can be acquired either independently (40) or associated with MRF data (52). Slice profile can be simulated and modeled into MRF dictionary (53). To avoid slice profile imperfections, spiral acquisition-based 3D MRF has been demonstrated (39,40). Furthermore, 3D volume excitation increased SNR could also benefit characterization of low spin density tissues like bone. Second, although T_2 of cortical bone from the chosen ROI is in agreement with previous work (19), cortical bone quantification in Fig. 7 suffers from the strong streaking artifact from bone marrow. This issue could be solved via either separating water and fat before dictionary matching (34) or characterizing fat into MRF dictionary (31). Additionally, the experiment could be optimized via optimizing UTE-MRF FA and TE variations patterns (54). Third, ultrashort T_2 components from myelin membrane or membrane structures in white matter and gray matter are explored by previous UTE methods (55,56). With TE of 0.05 ms, UTE-MRF acquires those ultrashort T_2 components, however, this phenomenon was not fully studied in this work.

Conclusion

An ultrashort echo time MR fingerprinting (UTE-MRF) method with sinusoidal echo time variations was proposed and tested via simulation, phantom and in vivo experiments. Its capability to quantify tendon and cortical bone could benefit quantification of bone water concentration for age-related bone degradations and other musculoskeletal abnormalities. Furthermore, UTE-MRF could be used in PET/MRI system to simultaneously quantify brain and aid PET attenuation correction with simultaneously synthesized pseudo-CT images.

Acknowledgment

This work was supported by the National Key R&D Program of China (2017YFC0909200, 2017YFE0104000, 2016YFC1300302), National Natural Science Foundation of China (81871428, 91632109, 81401473, 61701436, 61525106, 61427807), the Fundamental Research Funds for the Central Universities (2017QNA5016), Shenzhen Innovation Funding (JCYJ20170818164343304, JCYJ20170816172431715) and Shanghai Key Laboratory of Psychotic Disorders (13dz2260500).

References

1. Du J, Bydder GM. Qualitative and quantitative ultrashort-TE MRI of cortical bone. *NMR Biomed.* 2013;26:489–506.
2. Chang EY, Du J, Chung CB. UTE imaging in the musculoskeletal system. *J. Magn. Reson. Imaging.* 2015;41:870–883.
3. Boucneau T, Cao P, Tang S, Han M, Xu D, Henry RG, Larson PEZ. In vivo characterization of brain ultrashort-T2 components. *Magn. Reson. Med.* 2018;80:726–735.
4. Wiesinger F, Sacolick LI, Menini A, Kaushik SS, Ahn S, Veit-Haibach P, Delso G, Shanbhag DD. Zero TE MR bone imaging in the head. *Magn. Reson. Med.* 2016;75:107–114.
5. Larson PEZ, Han M, Krug R, Jakary A, Nelson SJ, Vigneron DB, Henry RG, McKinnon G, Kelley DAC. Ultrashort echo time and zero echo time MRI at 7T. *Magn. Reson. Mater. Physics, Biol. Med.* 2016;29:359–370.
6. Johnson EM, Vyas U, Ghanouni P, Pauly KB, Pauly JM. Improved cortical bone specificity in UTE MR Imaging. *Magn. Reson. Med.* 2017;77:684–695.
7. Emid S, Creyghton JHN. High Resolution NMR Imaging in Solids. *Physica B+ C.* 1985; 128(1): 81–83.

8. Balcom BJ, Macgregor RP, Beyea SD, Green DP, Armstrong RL, Bremner TW. Single-point ramped imaging with t1 enhancement (SPRITE). *J. Magn. Reson.* 1996; 123: 131–134.
9. Fernández-Seara MA, Wehrli SL, Wehrli FW. Multipoint mapping for imaging of semi-solid materials. *J. Magn. Reson.* 2003; 160(2): 144–150.
10. Grodzki DM, Jakob PM, Heismann B. Ultrashort echo time imaging using pointwise encoding time reduction with radial acquisition (PETRA). *Magn. Reson. Med.* 2012;67:510–518.
11. Froidevaux R, Weiger M, Brunner DO, Dietrich BE, Wilm BJ, Pruessmann KP. Filling the dead-time gap in zero echo time MRI: Principles compared. *Magn. Reson. Med.* 2018;79:2036–2045.
12. Manhard MK, Harkins KD, Gochberg DF, Nyman JS, Does MD. 30-Second bound and pore water concentration mapping of cortical bone using 2D UTE with optimized half-pulses. *Magn. Reson. Med.* 2017;77:945–950.
13. Ma YJ, Lu X, Carl M, Zhu Y, Szeverenyi NM, Bydder GM, Chang EY, Du J. Accurate T1 mapping of short T2 tissues using a three-dimensional ultrashort echo time cones actual flip angle imaging-variable repetition time (3D UTE-Cones AFI-VTR) method. *Magn. Reson. Med.* 2018; 80(2): 598–608.
14. Li X, Majumdar S. Quantitative MRI of articular cartilage and its clinical applications. *J. Magn. Reson. Imaging.* 2013; 38(5): 991–1008.
15. Williams A, Qian Y, Golla S, Chu CR. UTE-T2* mapping detects sub-clinical meniscus injury after anterior cruciate ligament tear. *Osteoarthr. Cartil.* 2012; 20(6): 486–494.
16. Abbasi-Rad S, Saligheh Rad H. Quantification of human cortical bone bound and free water in vivo with ultrashort echo time MR imaging: a model-based approach. *Radiology.* 2017;283:862–872.
17. Larson PE, Gurney PT, Nayak K, Gold GE, Pauly JM, Nishimura DG. Designing long-T2 suppression pulses for ultrashort echo time imaging. *Magn Reson Med.* 2006;56(1):94-103.

18. Johnson EM, Vyas U, Ghanouni P, Pauly KB, Pauly JM. Improved cortical bone specificity in UTE MR Imaging. *Magn. Reson. Med.* 2017; 77(2): 684-695.
19. Du J, Takahashi AM, Bae WC, Chung CB, Bydder GM. Dual inversion recovery, ultrashort echo time (DIR UTE) imaging: creating high contrast for short-T(2) species. *Magn. Reson. Med.* 2010;63(2):447-55.
20. Ma L, Meng Q, Chen Y, Zhang Z, Sun H, Deng D. Preliminary use of a double-echo pulse sequence with 3D ultrashort echo time in the MRI of bones and joints. *Exp Ther Med.* 2013;5(5):1471-1475.
21. Ma D, Gulani V, Seiberlich N, Liu K, Sunshine JL, Duerk JL, Griswold MA. Magnetic resonance fingerprinting. *Nature.* 2013; 495:187–192.
22. Liao C, Wang K, Cao X, Li Y, Wu D, Ye H, Ding Q, He H, Zhong J. Detection of Lesions in Mesial Temporal Lobe Epilepsy by Using MR Fingerprinting. *Radiology.* 2018; 172131.
23. Chen Y, Jiang Y, Pahwa S, Ma D, Lu L, Twieg MD, Gulani V, MR fingerprinting for rapid quantitative abdominal imaging. *Radiology,* 2016; 279(1): 278–286.
24. Rahmer J, Börnert P, Groen J, Bos C. Three-dimensional radial ultrashort echo-time imaging with T2 adapted sampling. *Magn. Reson. Med.* 2006;55(5):1075–1082.
25. Bernstein MA, King FK, Zhou XJ. Handbook of MRI pulse sequences. Burlington. MA: Elsevier Academic Press; 2004.
26. Jiang Y, Ma D, Seiberlich N, Gulani V, Griswold MA. MR fingerprinting using fast imaging with steady state precession (FISP) with spiral readout. *Magn. Reson. Med.* 2015;74(6):1621–1631.
27. Pauly JM. Selective Excitation for Ultrashort Echo Time Imaging. *Encycl. Magn. Reson.* 2012;1:381–388.
28. Nielsen HTC, Gold GE, Olcott EW, Pauly JM, Nishimura DG. Ultra-short echo-time 2D time-of-flight MR angiography using a half-pulse excitation. *Magn. Reson. Med.* 1999; 41(3): 591–599.
29. Du J, Hamilton G, Takahashi A, Bydder M, Chung CB. Ultrashort echo time spectroscopic imaging (UTESI) of cortical bone. *Magn. Reson. Med.*

- 2007;58(5):1001–1009.
30. Rieger B, Zimmer F, Zapp J, Weingärtner S, Schad LR. Magnetic resonance fingerprinting using echo-planar imaging: Joint quantification of T1 and T2* relaxation times. *Magn. Reson. Med.* 2017;78:1724–1733.
 31. Cencini M, Biagi L, Kaggie JD, Schulte RF, Tosetti M, Buonincontri G. Musculoskeletal MR Fingerprinting with dictionary-based fat and water separation. In Proceedings of the 26th Annual Meeting of ISMRM, Paris, 2018. Abstract 1025.
 32. Hennig J, Weigel M, Scheffler K. Calculation of Flip Angles for Echo Trains with Predefined Amplitudes with the Extended Phase Graph (EPG)-Algorithm: Principles and Applications to Hyperecho and TRAPS Sequences. *Magn. Reson. Med.* 2004; 51(1): 68–80.
 33. Weigel M. Extended phase graphs: dephasing, RF pulses, and echoes -pure and simple. *J. Magn. Reson. Imaging.* 2015; 41(2): 266-295.
 34. Koolstra K, Webb A, Koken P, Nehrke K, Bornert P. Water-Fat Separation in Spiral Magnetic Resonance Fingerprinting using Conjugate Phase Reconstruction. In Proceedings of the 26th Annual Meeting of ISMRM, Paris, 2018. Abstract 681.
 35. Rappaport TS. *Wireless communications: principles and practice.* prentice hall PTR New Jersey; 1996.
 36. Cao X, Liao C, Wang Z, Chen Y, Ye H, He H, Zhong J. Robust sliding-window reconstruction for Accelerating the acquisition of MR fingerprinting. *Magn. Reson. Med.* 2017; 78(4): 1579–1588.
 37. Li Q, Cao X, Ye H, Liao C, He H, Zhong J. Quantification of long and ultra-short relaxation times in tissues with ultra-short TE MR fingerprinting (UTE-MRF). In Proceedings of the 26th Annual Meeting of ISMRM, Paris, 2018. Abstract 680.
 38. Cloos MA, Knoll F, Zhao T, Block KT, Bruno M, Wiggins GC, Sodickson DK. Multiparametric imaging with heterogeneous radiofrequency fields. *Nat. Commun.* 2016;7:1–10.
 39. Liao C, Bilgic B, Manhard MK, Zhao B, Cao X, Zhong J, Wald LL, Setsompop K. 3D MR fingerprinting with accelerated stack-of-spirals and hybrid sliding-window

- and GRAPPA reconstruction. *Neuroimage* 2017; 162: 13-22.
40. Ma D, Jiang Y, Chen Y, McGivney D, Mehta B, Gulani V, Griswold M. Fast 3D magnetic resonance fingerprinting for a whole-brain coverage. *Magn. Reson. Med.* 2018;79(4):2190–2197.
 41. Fessler JA, Sutton BP. Nonuniform fast Fourier transforms using min-max interpolation. *IEEE Trans. Signal Process.* 2003;51:560-574.
 42. Walsh DO, Gmitro AF, Marcellin MW. Adaptive reconstruction of phased array MR imagery. *Magn. Reson. Med.* 2000;43(5):682–690.
 43. Deshmane A, McGivney D, Badve C, Gulani V, Griswold M. Dictionary approach to partial volume estimation with MR fingerprinting: validation and application to brain tumor segmentation. In *Proceedings of the 25th Annual Meeting of ISMRM, Honolulu, 2017*. Abstract 132.
 44. Gold GE, Han E, Stainsby J, Wright G, Brittain J, Beaulieu C. Musculoskeletal MRI at 3.0 T: Relaxation times and image contrast. *Am. J. Roentgenol.* 2004;183:343–351.
 45. Manhard MK, Horch RA, Gochberg DF, Nyman JS, Does MD. In Vivo Quantitative MR Imaging of Bound and Pore Water in Cortical Bone. *Radiology* 2015;277:221–229.
 46. Zwart NR, Johnson KO, Pipe JG. Efficient sample density estimation by combining gridding and an optimized kernel. *Magn. Reson. Med.* 2012; 67(3): 701–710.
 47. Hargreaves BA, Cunningham CH, Nishimura DG, Conolly SM. Variable-rate selective excitation for rapid MRI sequences. *Magn. Reson. Med.* 2004;52(3):590–597.
 48. Wundrak S, Paul J, Ulrici J, Hell E, Rasche V. A small surrogate for the golden angle in time-resolved radial MRI based on generalized fibonacci sequences. *IEEE Trans. Med. Imaging* 2015;34:1262–1269.
 49. Barral, J. K., Gudmundson, E. , Stikov, N. , Etezadi -Amoli, M. , Stoica, P. and Nishimura, D. G. (2010), A robust methodology for in vivo T1 mapping. *Magn. Reson. Med.*, 64: 1057-1067.

50. Chen, J., Carl, M., Ma, Y., Shao, H., Lu, X., Chen, B., Du, J., Fast volumetric imaging of bound and pore water in cortical bone using three -dimensional ultrashort -TE (UTE) and inversion recovery UTE sequences. *NMR in Biomed.* 2016; 29(10), 1373–1380.
51. Juras, V., Apprich, S., Szomolanyi, P., Bieri, O., Deligianni, X., Trattnig, S. Bi-exponential T2* analysis of healthy and diseased Achilles tendons: an in vivo preliminary magnetic resonance study and correlation with clinical score. *European radiology* 2013; 23(10): 2814–2822.
52. Buonincontri G, Sawiak SJ. MR fingerprinting with simultaneous B1 estimation. *Magn. Reson. Med.* 2016;76(4):1127–1135.
53. Ma D, Coppo S, Chen Y, McGivney DF, Jiang Y, Pahwa S, Gulani V, Griswold MA. Slice profile and B1 corrections in 2D magnetic resonance fingerprinting. *Magn. Reson. Med.* 2017;78(5):1781–1789.
54. Zhao, B., Haldar, J.P., Liao, C., Ma, D., Jiang, Y., Griswold, MA., Setsompop, K. and Wald, LL., Optimal experiment design for magnetic resonance fingerprinting: Cramer-Rao bound meets spin dynamics. *IEEE transactions on medical imaging.* 2018.
55. Horch R A, Gore J C, Does M D. Origins of the ultrashort -T2 1H NMR signals in myelinated nerve: a direct measure of myelin content?[J]. *Magnetic resonance in medicine*, 2011, 66(1): 24-31.
56. Fan SJ, Ma Y, Chang EY, Bydder GM, Du J. Inversion recovery ultrashort echo time imaging of ultrashort T2 tissue components in ovine brain at 3 T: a sequential D2O exchange study. *NMR in Biomedicine.* 2017;30:e3767.

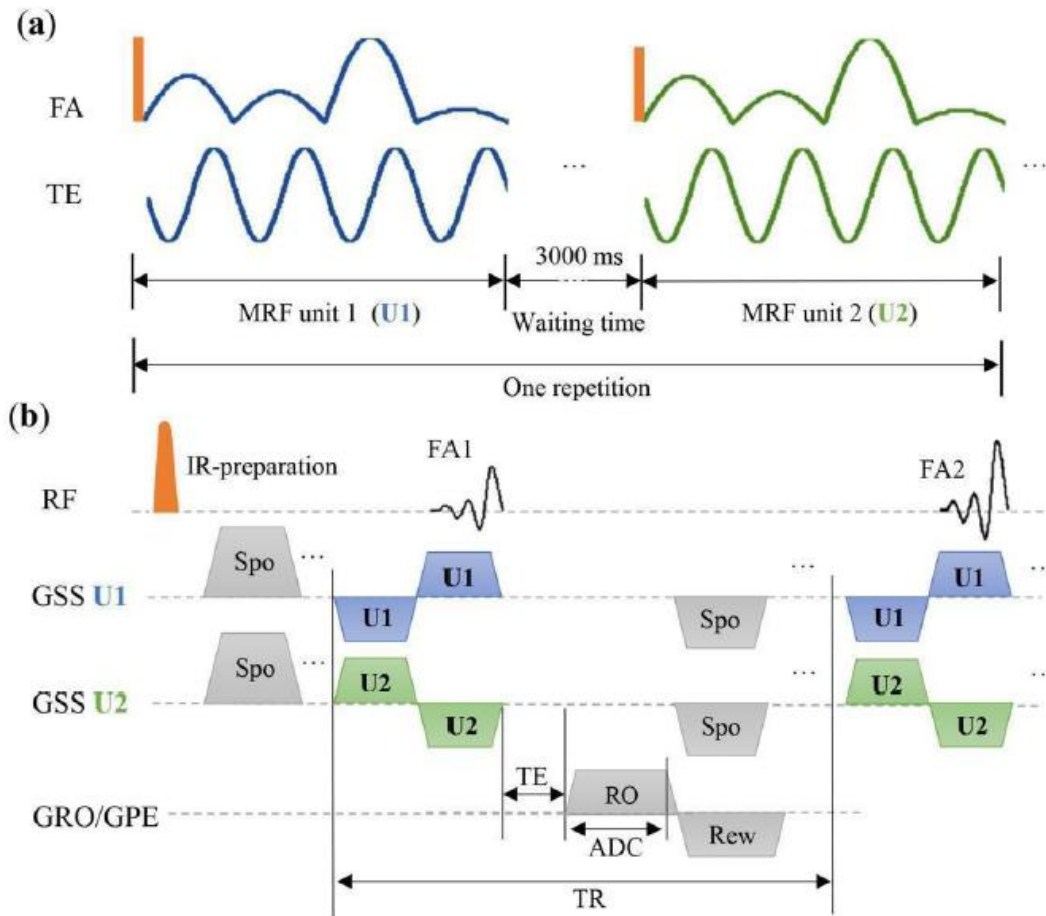


Fig. 1, Sequence diagram of UTE-MRF. UTE-MRF are acquired with IR-FISP sequence associated with half pulse excitation and radial acquisition. A fingerprint-like scan shown in (a) is called a MRF unit, where flip angle and echo time varies from TR to TR. A fixed repetition time of 6 ms was used to increase scan efficiency. One UTE-MRF repetition comprises both MRF units. Details of RF and gradient timing in a single TR is shown in (b). Slice selection gradient polarization is fixed within one MRF unit (U1, in blue), but inverts for the next MRF unit (U2, in green). k-Space trajectories of the same MRF frame are uniformly distributed over a unit circle when multiple repetitions are performed. Spo, RO, Rew are short for the gradients of spoiler, readout, and rewinder.

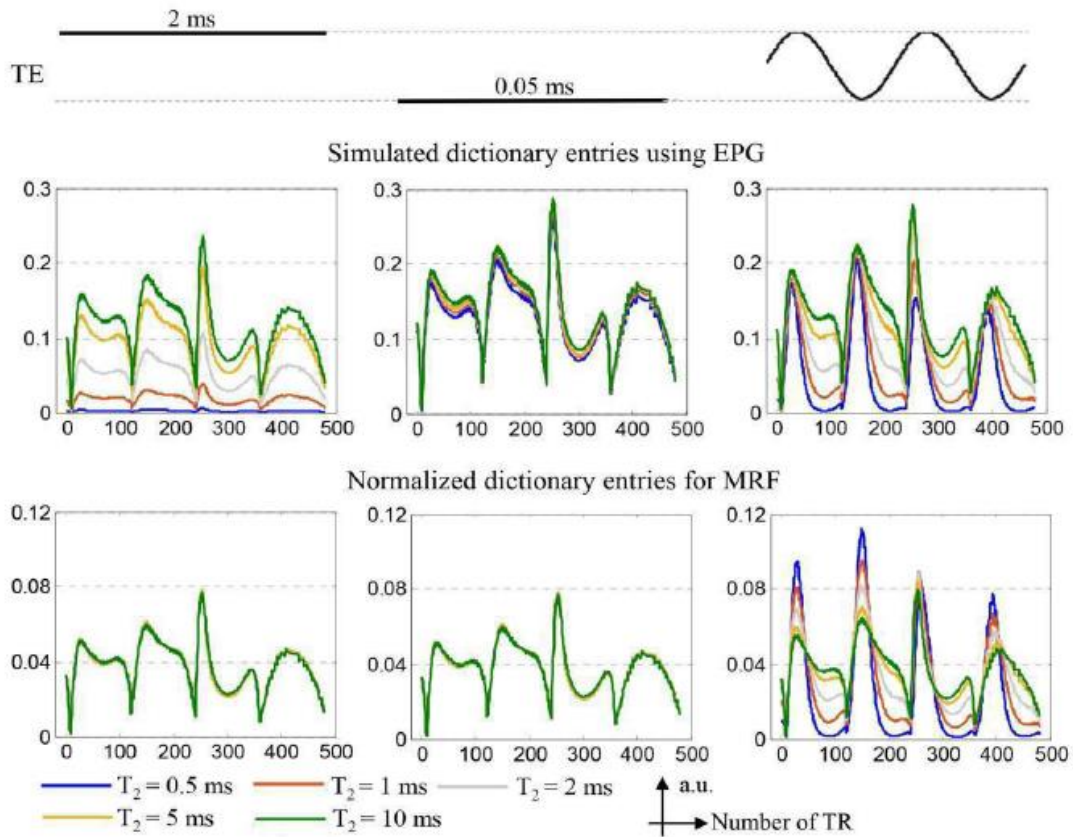
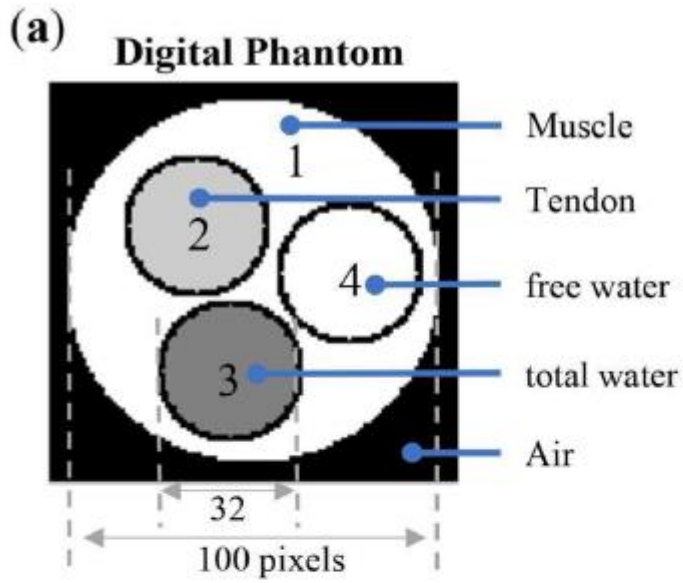


Fig. 2, Simulations of the impact of TE patterns to MRF signal evolutions (fingerprints) under the same T_1 of 180 ms and increased T_2 of 0.5, 1, 2, 5, and 10 ms. Two single TEs of 2 and 0.05 ms are respectively used in the first and second columns. In the last column TE varies in a sinusoidal pattern from 0.05 to 2 ms. For dictionary entries at constant TEs (the first two columns), the difference among simulated fingerprints (second row) disappears after dictionary normalization (last row). However, these fingerprints under sinusoidal TE can be differentiated both before and after dictionary normalization (last column).



(b) Tissue Parameters

	T_1 (ms)	T_2 (ms)	T_2^* (ms)	PD	SNR
Muscle	1400	32	114	1	28
Tendon	621	3	9.9	0.8	20
Total water	246	1.2	1.7	0.7	14
Free water	524	3.5	7.6	0.3	7

Fig. 3, Digital phantom and its corresponding simulation parameters. The peripheral cylinder is with diameter of 100 (pixels) and the inserted small cylinders are with diameter of 32 (pixels). Tissue parameters are chosen based on literatures (19,44,45). T_2^* values are 25 ms for muscle, 2.3 ms for tendon, 0.7 ms for total water, and 2.4 ms for free water.

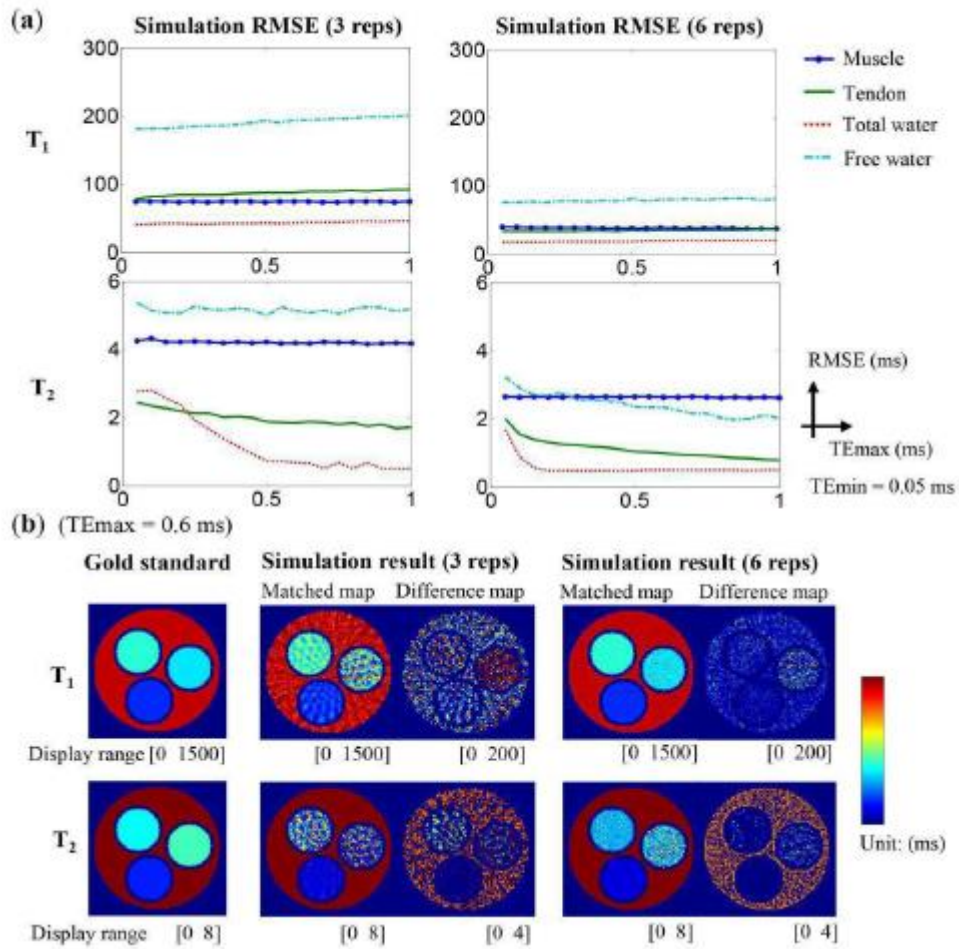


Fig. 4, Simulation results of the digital phantom with increased TE sampling ranges depending on maximum TE (TE_{max}), where TE_{min} = 0.05 ms and TE_{max} increases from 0.05 to 1 ms in steps of 0.05 ms. (a) shows the comparisons of averaged quantification errors for each tissue under 3 and 6 repetitions (reps). With the increase of TE sampling range, decreases in T₂ quantification errors for tendon, total water, and free water are observed. Meanwhile, T₁ and T₂ quantification performances for long T₂ muscle are almost unchanged. (b) shows an example of reconstructed T₁ and T₂ maps under TE_{max} of 0.6 ms and their comparisons with gold standards. Streaking artifacts from undersampled radial trajectory in 3 reps are largely reduced with 3 more reps.

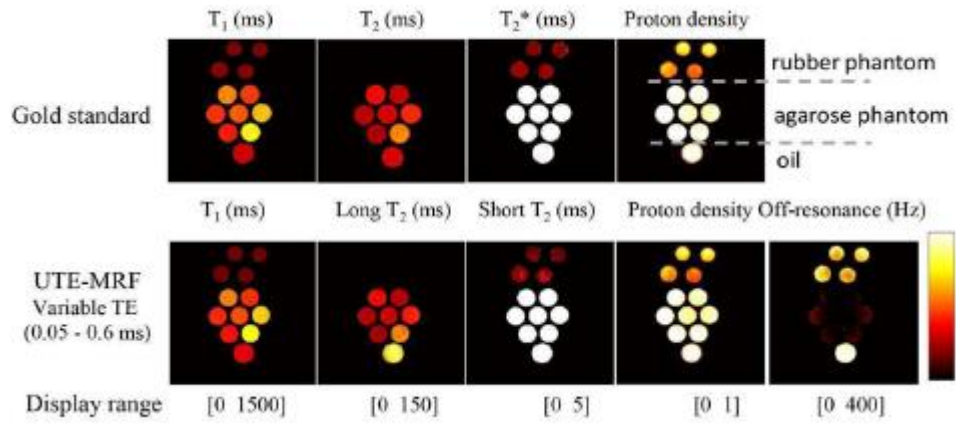


Fig. 5, Comparisons of multiple parametric maps between UTE-MRF($T_{Emin} = 0.05$ ms and $T_{Emax} = 0.6$ ms) and gold standards. T_2 maps from UTE-MRF are displayed in the range of 0 to 5 ms and compared with gold standard T_2^* map in the third column. PD maps are normalized by their peak amplitude.

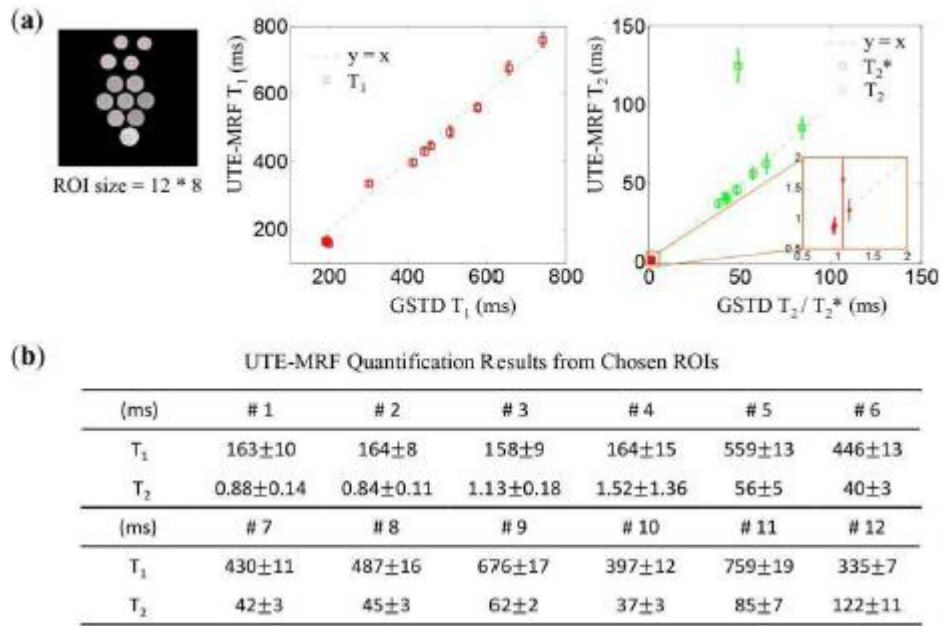


Fig. 6, Comparisons of T₁ and T₂ quantifications between UTE-MRF (TE_{min} = 0.05 ms and TE_{max} = 0.6 ms) and gold standard from chosen ROIs. (a) Plots of T₁ and T₂ from UTE-MRF versus gold standard in twelve chosen ROIs (red boxes, size of 12 x 8 pixels), where T₂ values of rubber phantom are compared with gold standard T₂* (red marker) and T₂ values of agarose phantom are compared with gold standard T₂ (green marker). (b) T₁ and T₂ in UTE-MRF (mean±SD) from chosen ROIs, where ROIs from left to right and from top to bottom are numbered sequentially from 1 to 12. As shown in Fig 5, #1-4 are for rubber plugs, #5-11 are for agarose tubes, and #12 is for oil tube.

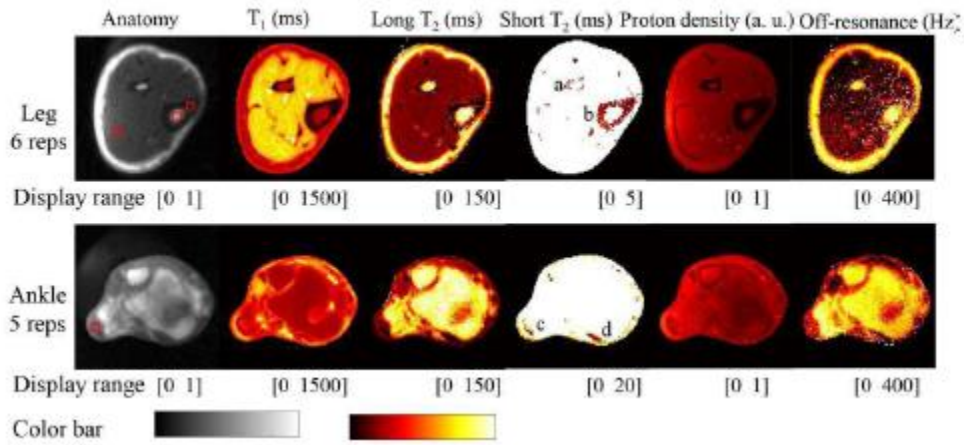


Fig. 7, In vivo results of leg and ankle (resolution = $1.0 \times 1.0 \text{ mm}^2$). Images are acquired with $T_{Emin} = 0.05 \text{ ms}$, $T_{Emax} = 0.6 \text{ ms}$, TE variation period = 120, and reps = 6 for leg and 5 for ankle. Tibia (a), fibula (b), Achilles tendon (c), and peroneus longus tendon (d) are detected and quantified in the fourth column. Two 5×5 ROIs are selected among muscle and bone marrow and 3×3 ROIs among fibula and Achilles tendon. The average T_2 value is 1.0 ms in the chosen fibula and 15 ms in the Achilles tendon.

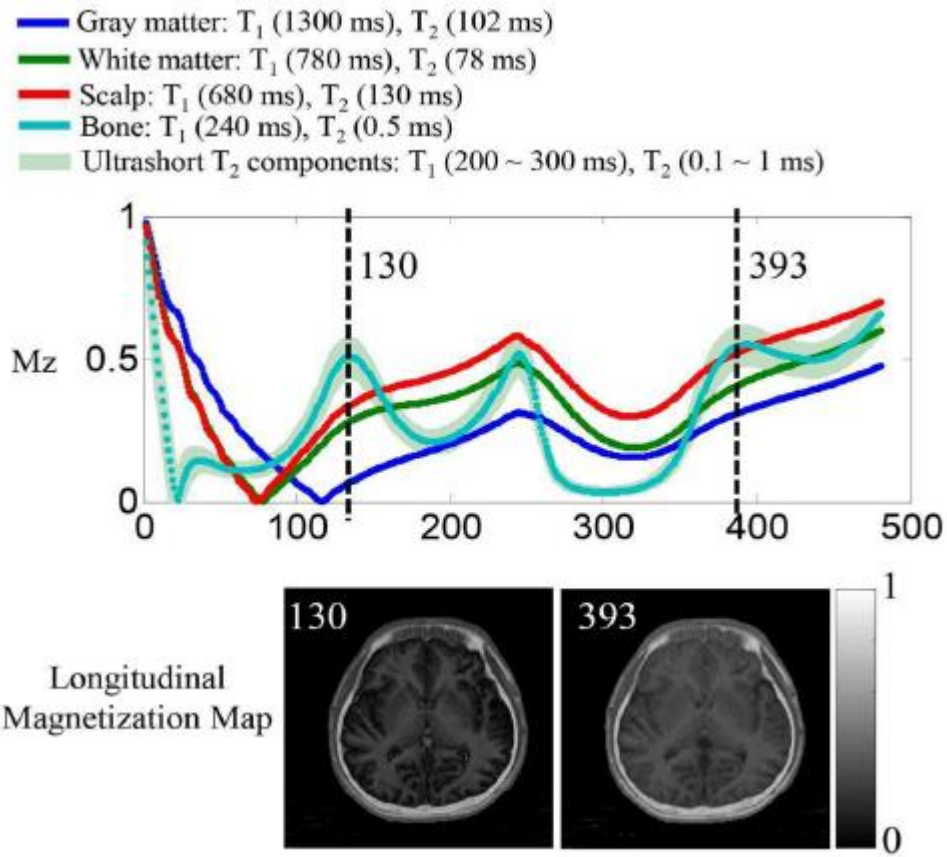


Fig. 8, Simulations of longitudinal magnetization for bone and soft tissue in the brain using EPG. Longitudinal magnetization maps at MRF No. 130 and 393 are displayed at the bottom, where bone is highlighted.

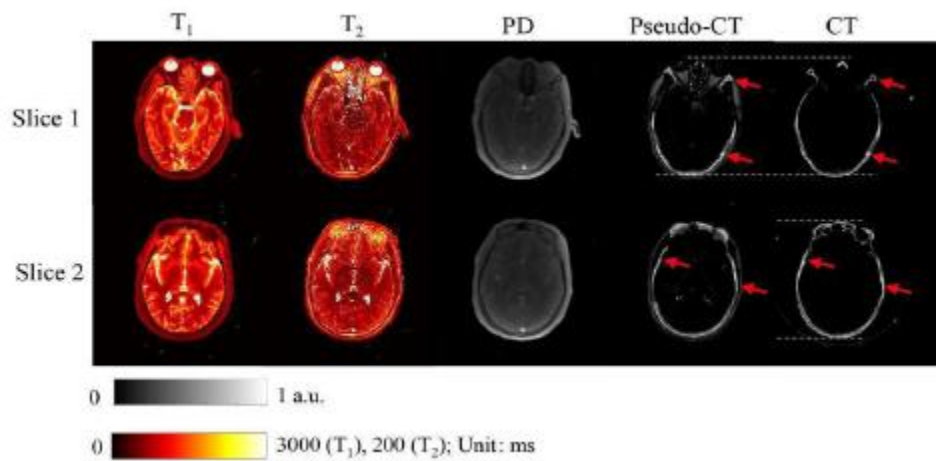


Fig. 9, Pseudo-CT (pCT) images, T_1 , T_2 , and PD maps from a volunteer using 5 UTE-MRF reps and constant TE of 0.05 ms (resolution = $0.75 \times 0.75 \text{ mm}^2$). Soft tissues in pCT images are highly suppressed compared to the longitudinal magnetization maps in Fig. 8. Bone structures produced by UTE-MRF are in good agreement with CT images especially the bone density variations as red arrows pointed.